Atmospheric
Chemistry
and Physics
Discussions

Continental-scale contributions to the global CFC-11 emission increase between 2012 and 2017

Lei Hu[1,2], Stephen A. Montzka[2], Fred Moore[1,2], Eric Hintsa[1,2], Geoff Dutton[1,2], M. Carolina Siso[1,2], Kirk Thoning[2], Robert W. Portmann[3], Kathryn McKain[1,2], Colm Sweeney[2], Isaac Vimont[1,2], David Nance[1,2], Bradley Hall[2], Steven Wofsy[4]

[1] Cooperative Institute for Research in Environmental Sciences, University of Colorado-Boulder, Boulder, CO, USA
[2] Global Monitoring Laboratory, NOAA, Boulder, CO, USA
[3] Chemical Science Laboratory, NOAA, Boulder, CO, USA
[4] Department of Earth and Planetary Sciences, Harvard University, Boston, MA, USA

Correspondence to: Lei Hu (lei.hu@noaa.gov)

Abstract. The early detection of a global emission increase of CFC-11 after 2012 (Montzka et al., 2018) alerted society to a possible violation of the Montreal Protocol on Substances that Deplete the Ozone Layer (MP). This early alert resulted in parties participating in the MP taking urgent actions (United Nations Environment Programme (UNEP), 2019). As a result, atmospheric measurements made in 2019 suggest a sharp decline in global CFC-11 emissions (Montzka et al., 2021). Despite the success in the early detection and mitigation of some of this problem, regions fully responsible for the recent global emission changes of CFC-11 have not yet been identified. Roughly two thirds (60 ± 40 %) of the emission increase between 2008 - 2012 and 2014 - 2017 and two thirds (60 ± 30 %) of emission decline between 2014 - 2017 and 2019 was explained by regional emission changes in eastern mainland China (Park et al., 2021; Rigby et al., 2019). Here, we used atmospheric CFC-11 measurements made from two global aircraft surveys, the HIAPER Pole-to-Pole Observations (HIPPO) in November 2009 – September 2011 and the Atmospheric Tomography Mission (ATom) in August 2016 – May 2018, in combination with the global CFC-11 measurements made by the U.S. National Oceanic and Atmospheric Administration during these two periods, to derive global and regional emission changes of CFC-11. Our results suggest Asia accounted for the largest fractions of global CFC-11 emissions in both periods, 43 (37 – 52) % during November 2009 – September 2011 and 57 (49 – 62) % during August 2016 – May 2018. Asia was also primarily responsible for the emission increase between these two periods, accounting for 86 (59 – 115) % of the global CFC-11 emission rise between the two periods. Besides eastern mainland China, we find that temperate western Asia and tropical Asia also contributed significantly to global CFC-11 emissions during both periods and likely to the global CFC-11 emission increase between these periods. Besides Asia, the atmospheric observations also provide strong constraints on CFC-11 emissions from North America and Europe, suggesting that each of them accounted for 10 – 15 % of global CFC-11 emissions during the HIPPO period and smaller fractions in the ATom period. For South America, Africa, and Australia, the derived regional emissions had larger dependence on the prior assumptions of emissions and emission changes, due to a lower sensitivity of the observations considered here to emissions from these regions. However, significant increases in CFC-11 emissions from the southern hemispheric lands

45   were not likely due to the observed increase of north-to-south interhemispheric gradients in
46   atmospheric CFC-11 mole fractions from 2012 to 2017.
47
48   **1. Introduction**
49   Trichlorofluoromethane, CFC-11, is a potent ozone depleting substance, whose production
50   has been controlled by the Montreal Protocol since 1987. By 2010, reported global production
51   and consumption of CFC-11 was near zero (United Nations Environment Programme (UNEP),
52   2021a, b). Corresponding to the declining production and consumption, global emissions of CFC-
53   11 declined between 1988 and 2012. By 2012, the global CFC-11 emission magnitude was 50 –
54   80 Gg yr^{-1} with this range being associated primarily with its uncertain atmospheric lifetime (Engel
55   et al., 2018). The remaining emissions of CFC-11 were primarily from existing equipment and
56   insulation foams, known as "CFC-11 banks". However, a large increase of global CFC-11
57   emission from 2012 – 2017 was discovered (Montzka et al., 2018; Rigby et al., 2019; Montzka et
58   al., 2021), suggesting illicit CFC-11 production despite the global ban on production and
59   consumption under the MP beginning in 2010. This surprisingly large increase of CFC-11
60   emissions attracted great attention from scientists, policy makers, industrial experts around the
61   world (Montzka et al., 2018; Rigby et al., 2019; Dhomse et al., 2019; Ray et al., 2020; Adcock et
62   al., 2020; Keeble et al., 2020; Chen et al., 2020), who sought information to enable rapid mitigation
63   of the unexpectedly enhanced CFC-11 emissions and ensure no significant delay in the recovery
64   of stratospheric ozone. Despite the international effort to understand the origin of this large global
65   emission increase of CFC-11, only a portion of the emission rise (60 ± 40 %) could be explained
66   by emission increases from eastern mainland China (Rigby et al., 2019; Adcock et al., 2020; Park
67   et al., 2021). It remains unclear where the rest of the global CFC-11 emission increase originated.
68   Following the initial studies and announcements of anomalous CFC-11 emission increases,
69   a surprisingly sharp decline in global CFC-11 emissions occurred from 2018 to 2019 (Montzka et
70   al., 2021). This decline immediately followed the global emission rise and had a similar magnitude
71   as the emission rise between 2012 and 2017, resulting in the global CFC-11 emission dropping to
72   the mean 2008 – 2012 value (Montzka et al., 2021). Interestingly, roughly the same proportion of
73   this emission decrease (60 ± 30 %) can be explained by an emission drop in eastern mainland
74   China (Park et al., 2021) during this period, as the contribution of eastern mainland China to the
75   global CFC-11 emission rise earlier (60 ± 40 %).
76   In this study, we analyzed global CFC-11 measurements made from the HIAPER Pole-to-
77   Pole Observations (HIPPO) in November 2009 – September 2011, the Atmospheric Tomography
78   Mission (ATom) in August 2016 – May 2018 (Wofsy, 2018; Bourgeois et al., 2020) and concurrent
79   CFC-11 measurements from the NOAA's global atmospheric sampling network (Montzka et al.,
80   2018) and combined them with Lagrangian-based inverse modeling techniques (Hu et al., 2017)
81   to quantify continental- and regional- scale CFC-11 emission estimates between both periods.
82   Coincidentally, the timing of the HIPPO and ATom campaigns covered the periods when the
83   global CFC-11 emissions were at the minimum and maximum before the CFC-11 emission decline
84   in 2018 – 2019. Hereafter, we will refer November 2009 – September 2011 as the HIPPO period
85   and August 2016 – May 2018 as the ATom period. Here we further investigate regional
86   contributions to the global CFC-11 emission rise between these two periods.
87
88   **2. Methods**
89   **2.1. Overview**

90   To infer regional CFC-11 emissions from observed atmospheric mole fractions, we used a
91   Bayesian inverse modeling framework following the method described in our previous studies (Hu
92   et al., 2015; Hu et al., 2017; Hu et al., 2016). In brief, the inverse modeling method assumes a
93   linear relationship between atmospheric mole fraction enhancements and upwind emissions. The
94   linear operator is footprints or the sensitivities of atmospheric mole fraction changes to upwind
95   emission regions that were computed by time-inverted Lagrangian particle models described in
96   Stein et al. (2015) and Nehrkorn et al. (2010). Because the inverse problem we generally solve is
97   not fully constrained by the available number of atmospheric observations, the solution in a
98   Bayesian inversion (Rodgers, 2000) requires initial assumptions about the magnitudes and
99   distributions of emissions or prior emissions. By assuming that errors between the "true" and prior
100 emissions and errors between atmospheric mole fraction observations and simulated mole fractions
101 (using the computed footprints) follow Gaussian distributions, we construct a cost function (L)
102 (Eq. 1) based on the Bayes' Theorem:

103
$$L = \frac{1}{2}(z - Hs)^T R^{-1}(z - Hs) + \frac{1}{2}\left(s - s_p\right)^T Q^{-1}\left(s - s_p\right) \tag{1}$$

104 where, z represents the observed atmospheric enhancement relative to the upwind background
105 atmosphere. s_p and s represent the prior and posterior CFC-11 emissions. H represents the Jacobian
106 matrix or the first-order partial derivatives of z to s. R and Q stand for the model-data mismatch
107 covariance and prior flux error covariance. The values given to R and Q determine the relative
108 weight between the prior emission assumptions and atmospheric observations in the final solution.
109 Here, we used the maximum likelihood estimation method (Hu et al., 2015; Michalak et al., 2005)
110 and atmospheric observations to directly solve for site-dependent model-data mismatch errors and
111 prior flux errors. For the aircraft campaigns (HIPPO and ATom), we derive separate model-data
112 mismatch errors, one for each campaign.
113

2.2. Inversions for the HIPPO and ATom periods

115 In this section, we describe the detailed observation selection, background mole fraction
116 estimation that was pre-subtracted from atmospheric observations before inversions, and prior
117 emission assumptions for the global inversion we conducted for the HIPPO period and the ATom
118 period using a Lagrangian inverse modeling approach.
119

2.2.1. CFC-11 measurements and data selection for global inversion analyses

121 All the CFC-11 measurements considered in our global inversion were made by the Global
122 Monitoring Laboratory, NOAA, through four different sampling and measurement programs: the
123 global aircraft surveys (flask samples collected during HIPPO and ATom), a global weekly surface
124 flask sampling program, a global in-situ sampling program, and a biweekly to monthly aircraft
125 profiling sampling program focused primarily in North America (Fig. 1). CFC-11 measurements
126 for the ATom campaigns were primarily made by a gas chromatography and mass spectrometry
127 (GCMS) instrument (named "M3") that was also dedicated for flask-air measurements in the
128 global weekly surface flask program. Flask-air samples collected from the biweekly to monthly
129 aircraft profiling sampling program and from the HIPPO campaign were analyzed by another
130 dedicated GCMS instrument called "M2" and later upgraded to "PR1" in Sep 2014. Hourly in situ
131 CFC-11 measurements were made by in situ gas chromatography with electron capture detector
132 instruments (GC-ECDs) located at individual observatories (the Chromatograph for Atmospheric
133 Trace Species, CATS). All the NOAA CFC-11 measurements were referenced to the same
134 calibration scale (NOAA-2016) and suite of primary gravimetric standards. However, small

135 differences were observed in measurements made from the same air samples that were analyzed
136 by two different instruments (i.e., median differences: 0.7% between M3 and M2 during the
137 HIPPO period and 0.9% between M3 and PR1 during ATom period; Fig. S1) or measurements
138 made for samples collected within ± 2 hours that were analyzed by M3 flask-air measurements
139 and CATS in situ measurements, i.e., median differences < 0.2% during the HIPPO and ATom
140 periods at three relevant sites (Fig. S1). To minimize the influence of these artificial differences
141 on derived fluxes, particularly because the atmospheric CFC-11 signals associated with changing
142 emissions were extremely small (Montzka et al., 2021; Montzka et al., 2018), results from M2 and
143 PR1 were scaled to those from M3. Scaling factors were calculated over 3-month intervals for M2
144 and PR1 to make them consistent for the same air-sample analyses. For the CATS measurements,
145 fewer comparison points were available, so scale adjustments to M3 were based on one scaling
146 factor per site for the HIPPO period and the ATom period, considered separately and derived from
147 the collocated measurements collected within ± 2 hours.
148   For measurements made during the HIPPO and ATom campaigns, we only include
149 measurements below 8 km in the global inversions to minimize the influence of stratospheric loss
150 on measured mole fractions and because high altitude samples typically have less emission
151 information. Some samples obtained below 8 km still retained a notable stratospheric loss signal,
152 and these data were also removed from further considerations on the basis of reduced mole
153 fractions observed for N_2O, which is useful for tracing stratospheric influence in an air parcel
154 owing to its small atmospheric variability and high-precision measurements.
155   For data obtained in our regular flask-air sampling programs, the inversions included
156 results from sites that are relatively away from recent emissions, in order to capture emissions
157 from broad regions. These observations include the weekly surface flask sampling at remote,
158 globally-distributed locations (Fig. 1) and aircraft profiling in Cook Islands and Alaska, US, and
159 above 1 km (above ground) over the contiguous US (Fig. 1). Most of our aircraft profiling
160 sampling was below 8 km above sea level.
161   To reduce the extremely large computing cost of footprint calculations for surface in situ
162 sampling, we chose a subset of in situ samples for inversion analyses. We randomly selected one
163 sample per day from sites such as Barrow, Alaska, US (BRW) and Tutuila, American Samoa
164 (SMO), and one daytime sample and one nighttime sample each day at Mauna Loa Observatory,
165 Hawaii, US (MLO). In situ measurements made at Summit, Greenland (SUM) were excluded due
166 to poor precision of CFC-11 measurements made at this station.
167   Although many of the observations we used were from remote Pacific and Atlantic Oceans
168 locations, or from the free troposphere over North America, they did contain above-zero sensitivity
169 to emissive signals transported from all the continents, as shown in their footprints (Fig. 1); but
170 the overall sensitivity to emissions from South America, southern Africa, and Australia is low
171 relative to North American, Europe, and Asia (Fig. 1). Thus, observational constraints on
172 emissions from North America, Europe, and Asia are stronger and have reduced dependence on
173 prior assumptions compared to those from South American, Africa, and Australia.

174 **2.2.2. Footprint simulations**
175   We used the Hybrid Single-Particle Lagrangian Integrated Trajectory (HYSPLIT) model
176 driven by the global data assimilation system at a 0.5° resolution (GDAS0.5°), to simulate
177 footprints for our global inversion analyses. To determine an adequate number of particles needed
178 for this global simulation, we tested running HYSPLIT backward for 45 days using 5000 and
179 10000 particles for a subset of observations obtained from the second campaign during ATom

180   (ATom II). We compared the footprints from these two independent simulations, which are only
181   different by < 0.05% in the total summed sensitivities. Footprint distributions and magnitudes in
182   individual time steps are also almost identical, suggesting using 5000 particles was adequate for
183   our global simulation.
184   To determine an adequate time duration for each HYSPLIT simulation, we compared
185   footprints for observations with enhanced CFC-11 mole fractions versus those with relatively low
186   mole fractions for observations made at different altitudes and latitudes from ATom II. Our results
187   show that, for observations in all altitudes and latitudes bins, those with enhanced CFC-11 mole
188   fractions always had higher sensitivity to upwind populated regions in the first 20 days (Fig. S2);
189   after that, the overall sensitivity was relatively small and constant, likely due to evenly distributed
190   particles throughout the troposphere beyond 20 days. This result suggests running HYSPLIT for
191   more than 20 days was likely sufficient for capturing the major emission influence on atmospheric
192   CFC-11 mole fraction observations made over the remote atmosphere. In the analysis presented
193   here, sensitivities were derived with HYSPLIT-GDAS0.5° by tracking 5000 particles back in time
194   for 30 days.

2.2.3. Estimation of background mole fractions

197   Emissions are derived from the Lagrangian analysis from measured mole fraction
198   enhancements above background values. For each observation, the background mole fraction was
199   estimated based on the 5000 HYSPLIT-GDAS0.5° back-trajectories and a background mole
200   fraction field. We derived several background mole fraction fields for comparison. Initially, we
201   examined the modeled 4D monthly CFC-11 mole fractions from the Whole Atmosphere
202   Community Climate Model (WACCM) (Davis et al., 2020; Marsh et al., 2013; Montzka et al.,
203   2021; Ray et al., 2020). In the WACCM simulation, global mole fractions and distributions of
204   CFC-11 were initialized in the year 1980. The WACCM model was run using version 1.2.2 with
205   interactive chemistry in the specified dynamics configuration at a resolution of 1.9° latitude × 2.5°
206   longitude horizontal with 88 vertical levels from Earth's surface to 6×10^{-6} hPa. Horizontal winds
207   and temperatures were nudged to specified dynamics derived from the Modern Era Retrospective-
208   analysis for Research and Applications (MERRA2). Compared to the ATom observations, these
209   WACCM forward simulations show 2 ppt positive average biases (Fig. S3), with larger biases in
210   the higher northern latitudes (~ 4 ppt). We also tried scaling this forward modelled background to
211   reduce its latitudinal bias. For this purpose, we calculated monthly, latitude-dependent scaling
212   factors every 30° in latitudes based on the ratios between the WACCM modeled average CFC-11
213   mole fractions below 3 km and the surface CFC-11 mole fractions observed by the NOAA's long-
214   term global weekly surface flask-air sampling network. This scaling allowed a reduction of
215   latitudinal biases in the WACCM simulations (Fig. S3), although a ~2 ppt bias still exists in the
216   equatorial region. As an alternative, we constructed an empirical 4D CFC-11 mole fraction field
217   based on NOAA observations. A 4D measurement-based background field was constructed by
218   propagating a subset of measured mole fractions of CFC-11 from the NOAA's global surface and
219   ongoing airborne flask-air sampling programs back in time along the 5000 back-trajectories for a
220   certain time duration. This subset of observations was selected given their measured mole fractions
221   were lower than a certain threshold in each 30° in latitude x 3 km in altitude box. We tested a
222   range of thresholds between the 40th and the 80th percentile in the HIPPO and ATom periods. We
223   ended up selecting observations lower than the 70 − 80th percentile in each box as background
224   observations during the HIPPO period and ones lower than 40 − 50th percentile as background

225   observations during the ATom period, so that the inversely derived global emissions in both
226   periods were consistent with those derived from the global 3 box model with different choices of
227   atmospheric lifetimes (Montzka et al., 2021). Although the inversely derived global emission
228   magnitudes were sensitive to the choice of the background threshold, the relative regional emission
229   distribution or the fraction of regional emissions to the global emission was not. By propagating
230   this subset of observations back in time, it provided a 4D field of CFC-11 mole fractions that we
231   then averaged every 5° latitude $\times$ 20° longitude $\times$ 2 km longitude every half or one month. We
232   tested the time duration of 10 – 30 days for propagating particles along the 5000 back-trajectories
233   and half or one month averaging time windows for estimating this empirical background. We
234   found propagating particles back in time for 10 days with an averaging window of one month can
235   produce a background field that best agrees with independent ATom and HIPPO observations
236   (Figs. S3 and S4). We further added the influence of stratospheric air on high altitude CFC-11
237   mole fractions (8 - 10 km) in the polar regions (> 60°N or > 60°S) to this empirical background,
238   by considering the vertical gradients simulated by WACCM over these regions. As a result, this
239   approach produced a background that best agreed with the ATom and HIPPO observations
240   compared to the previous two approaches (Figs. S3 and S4). Therefore, we used the 4D
241   background field derived from a subset of CFC-11 measurements in our final global inversion
242   simulations. Note that, the HIPPO and ATom campaign data were intentionally excluded and used
243   as independent assessment of the 4D background estimates at first; but they were later included in
244   the final 4D empirical background construction, after we confirmed that the empirical approach
245   produced the best estimate of background.
246   From the 4D measurement-based background mole fraction field, we sampled 5000 mole
247   fraction estimates at the locations of the 5000 back-trajectories at the end of the 30 days and then
248   averaged these 5000 mole fraction estimates to obtain one background mole fraction for each
249   observation. We examined the particle locations at the end of the 30 days using observations
250   collected at 0 - 8 km from ATom II. For the majority of these observations, 80% - 100 % of
251   particles were located between 0 and 10 km at the end of the 30 days in the HYSPLIT back-
252   trajectory runs. For particles that exited from the top at 10 km before 30 days, we sampled the
253   mole fractions at 10 km when they exited the background mole fraction field.
254
255   **2.2.4. Prior emissions**
256   We constructed 11 different prior emissions for inversion analyses in both HIPPO and
257   ATom periods (Fig. 2). The first prior, "population_67", was constructed with a global CFC-11
258   emission of 67 Gg yr^{-1} and the posterior emissions derived for the contiguous US (CONUS) from
259   Hu et al. (2017). Over the CONUS, the posterior annual 1° x 1° emissions derived for 2014 were
260   applied to all months in either HIPPO or ATom periods. We then subtracted the annual total
261   CONUS emissions (~ 4 Gg yr^{-1}) from the global total emission of 67 Gg yr^{-1} and distributed the
262   remaining emissions around the globe based on the Gridded Population of the World (GPW) v4
263   (https://sedac.ciesin.columbia.edu/data/collection/gpw-v4). The second prior, "population_40",
264   was the emission distribution in "population_67" with emission magnitudes reduced by 40%
265   across the globe. The priors "population_87_NA", "population_87_SA", "population_87_Af",
266   "population_87_Eu", "population_87_Au", "population_87_BA", "population_87_TEA",
267   "population_87_TWA", and "population_87_TA" incorporated the "population_67" prior and an
268   additional 20 Gg yr^{-1} of emission imposed over North America, South America, Africa, Europe,
269   Australia, boreal Asia, temperate eastern Asia, temperate western Asia, and tropical Asia,

270 respectively. The 20 Gg yr^{-1} of emissions was added to those regions by a constant emission rate
271 across all the grid cells where emissions were non-zero in the prior of "population_67". The
272 regions specified as North America, South America, Africa, Europe, Australia, boreal Asia,
273 temperate eastern Asia, temperate western Asia, and tropical Asia are shown in Fig. 3.

274 **2.2.5. Inversion ensembles**
275 We constructed 23 inversion ensembles for deriving global and regional emissions in the
276 HIPPO and ATom periods. These 23 inversion ensembles included 20 different prior emission
277 change scenarios between the HIPPO and ATom periods, two background CFC-11 mole fraction
278 fields, and two sets of observations ("flask only" and "flask + in situ") (Table S1). The 20 prior
279 emission change scenarios assumed: (scenario 1) no increase of global CFC-11 emissions between
280 the HIPPO and ATom periods (inversion ensemble IDs #1 - #5 in Table S1); (scenario 2) a 20 Gg
281 yr^{-1} increase of CFC-11 emissions between the HIPPO and ATom periods, with the increase being
282 restricted to one of the following regions, respectively: North America, South America, Africa,
283 Europe, Australia, boreal Asia, temperate eastern Asia, temperate western Asia, and tropical Asia
284 (inversion ensemble IDs #6 - #14 in Table S1); and (scenario 3) a 20 Gg yr^{-1} decrease of CFC-11
285 emissions between the HIPPO and ATom periods, with the decrease being restricted to one of the
286 following regions, respectively: North America, South America, Africa, Europe, Australia, boreal
287 Asia, temperate eastern Asia, temperate western Asia, and tropical Asia (inversion ensemble IDs
288 #15 - #23 in Table S1).
289 In our global inversions, we solved for monthly 1º x 1º emissions and their posterior
290 covariances at 1º x 1º resolution. Because the uncertainty associated with the 1º x 1º emissions is
291 large, we aggregated emissions and their posterior covariances into large regional, continental, and
292 global scales for the HIPPO and ATom periods, considering the cross correlation in errors among
293 grid cells and across times for each batch inversion (Hu et al., 2017).

295 **3. Results and Discussion**
296 **3.1. Increase of CFC-11 emissions between the HIPPO and ATom periods observed in remote**
297 **atmospheric observations**
298 The global increase of CFC-11 emissions between 2012 and 2017 was previously derived
299 from the slow-down in the decline of atmospheric CFC-11 mole fractions observed at Earth's
300 surface (Montzka et al., 2021; Montzka et al., 2018) and is also shown in Fig. 4 here. Besides at
301 Earth's surface, a similar magnitude of this slow-down in atmospheric CFC-11 mole fraction
302 decline is also apparent throughout the free troposphere in the aircraft profiles obtained during the
303 HIPPO and ATom campaigns (Fig. 4). Here, we calculated the CFC-11 growth rates averaged in
304 each 30º in latitude × 2 km in altitude box during HIPPO campaigns and during ATom campaigns
305 separately for samples collected above the Pacific Ocean basin. During HIPPO, we calculated the
306 average mole fraction differences in each 30º in latitude × 3 km in altitude box between HIPPO
307 III (3/2010 – 4/2010) and HIPPO IV (6/2011 – 7/2011) and normalized by their time interval to
308 obtain annual growth rates, whereas we calculated annual growth rates during ATom using the
309 ATom I (7/2016 – 8/2016) and ATom IV (4/2018 – 5/2018) data. The reason to choose HIPPO
310 III, HIPPO IV, ATom I, and ATom IV for this calculation is to ensure annual growth rates were
311 calculated from data collected in similar seasons, so that the impact of seasonal variations in
312 atmospheric CFC-11 mole fractions on the calculated annual growth rates was similar in both
313 periods (Fig. S5). Results suggest a median growth rate of -2.5 ppt yr^{-1} between 60ºS and 90ºN in

Atmospheric
Chemistry
and Physics
Discussions
Open Access
EGU

314 the troposphere during the HIPPO period and a median growth rate of -0.7 ppt yr^{-1} during the
315 ATom period (Fig. 4), indicating a significant increase of CFC-11 growth rates in the troposphere
316 between the HIPPO and ATom periods. The impact of atmospheric CFC-11 seasonal cycle
317 measured at the surface on the calculated changes of annual growth rates between both periods is
318 about ±0.1 ppt. Besides the seasonal cycle of atmospheric CFC-11 mole fractions, the Quasi-
319 Biennial Oscillation (QBO) can also influence atmospheric trace gas mole fractions in the
320 troposphere (Ray et al., 2020) and thus their growth rates; but this influence was smaller than the
321 increase of the annual growth rates between the HIPPO and ATom periods, as quantified in
322 Montzka et al. (2021).

323   Subtracting the background CFC-11 mole fractions from the selected global CFC-11
324 observations, there were enhancements up to 3 ppt measured in air above the Pacific Ocean basin
325 by the global HIPPO and ATom aircraft surveys, the global weekly flask sampling, and the
326 selected daily – to "every other day" in situ sampling (Fig. 5). Relatively larger enhancements
327 were more frequently measured during the ATom period than during the HIPPO period (Fig. 5).
328 However, the average increase in enhancements of the atmospheric CFC-11 mole fractions
329 measured during ATom were only 0.2 – 0.3 ppt higher than observed during the HIPPO campaign
330 (Fig. 5). The 0.2 – 0.3 ppt increase in the atmospheric CFC-11 enhancements were also
331 independently measured by the global weekly flask sampling, and in situ sampling networks over
332 the Pacific Ocean basin (Fig. 5). Results from HIPPO and ATom suggest that increased mole
333 fraction enhancements over the Pacific Ocean basin existed primarily between 0 and 60 ºN (Fig.
334 5), where the lower and middle tropospheric air mainly contains emissive signals from Eurasia,
335 western North America, and tropical America (Fig. S6). Furthermore, when comparing air over
336 the Pacific Ocean versus the Atlantic Ocean sampled by ATom, air above the Pacific Ocean basin
337 was more enhanced with CFC-11 than air above the Atlantic Ocean basin (Fig. 5), suggesting
338 regions immediately upwind of the Pacific Ocean may be emitted more CFC-11 than regions
339 upwind of the Atlantic Ocean (Fig. 1b) during the ATom period.

340
341 **3.2. Regional emissions derived from HIPPO and ATom global inversions**
342 **3.2.1. The base scenarios with only flask-air measurements**
343   To quantitatively understand what measured atmospheric CFC-11 variability implies for
344 global and regional CFC-11 emissions, we conducted Bayesian inversions as described above. We
345 first only used the flask-air measurements made by the two GCMS instruments. These
346 measurements include samples collected during HIPPO and ATom, the global weekly flask-air
347 sampling program, and the regular aircraft flask-air sampling program located primarily over
348 North America. The inversions derived from these flask-air measurements are referred to here as
349 "flask-only inversions". In this first base scenario, we used the same prior emission with a global
350 CFC-11 emission of 67 Gg yr^{-1} ("population_67") for both HIPPO and ATom periods (Table
351 S1). The global emissions derived from this scenario (67 $\pm$ 7 Gg yr^{-1} and 87 $\pm$ 9 Gg yr^{-1} for the
352 HIPPO and ATom periods) were based on background estimates that were calibrated against the
353 global 3-box model results, such that the global CFC-11 emissions derived from the grid-scale
354 inversions were consistent with those from the global 3-box model with an atmospheric lifetime
355 of 52 years reported by Montzka et al. (2021).

356   An inverse analysis of the flask data obtained during the HIPPO and ATom periods suggest
357 changes in the total magnitude and distribution of CFC-11 emissions from 2010 to
358 2018. Significant emission increases were derived for Asia, which we estimate was primarily

359 responsible for the global CFC-11 emission increase from 2010 to 2018. During the HIPPO period
360 (November 2009 – September 2011), Asia emitted 35 (±5) Gg yr^{-1} of CFC-11, accounting for
361 50% of global CFC-11 emissions, whereas Asian annual CFC-11 emissions increased to 51 (±8)
362 Gg yr^{-1} during the ATom period in August 2016 – May 2018, equal to 60% of the global CFC-11
363 emission at that time. The increase of CFC-11 emission from Asia during these two periods, 16
364 (±10) Gg yr^{-1}, accounted for 80 - 90 % of global CFC-11 emission increases (Fig. 6), as derived
365 from this scenario.
366   Our inversion results also suggest that the Asian CFC-11 emissions and emission increases
367 were primarily contributed by the temperate eastern Asia, temperate western Asia, and tropical
368 Asia in approximately equal amounts (Fig. 6). Correlations in the posterior emissions among these
369 three Asian subregions (r^2) were less than 0.1, suggesting the inversion was able to separate
370 regional total emissions from these three regions, although the derived analytical uncertainties
371 associated with emissions at the subregional level are large (Fig. 6).
372   Emissions derived for North America, South America, Africa, and Europe were 5 – 15 Gg
373 yr^{-1} for each region in both the HIPPO and ATom periods. Emissions derived for Australia were
374 less than 1 Gg yr^{-1}. Changes of CFC-11 emissions between both periods derived for these
375 continents from this scenario were smaller than their associated uncertainties.
376   With "flask-only" observations, we also tested the sensitivity of posterior regional
377 emissions to the prior emission magnitude. Here, we considered the second "population-density"
378 prior with a substantially lower global total CFC-11 emission of 40 Gg yr^{-1} for both periods
379 ("population_40") (Table S1). Derived regional emissions from this second scenario were
380 consistent with results discussed in the first scenario in both the distribution and total magnitude
381 of posterior emissions.

383 **3.2.2. Scenarios with more observations, prior assumptions, and an alternative background**
384   To increase the observational constraints in the global CFC-11 inversion, we then included
385 additional observations from the in-situ CFC-11 measurements (Fig. 1). The derived posterior
386 emissions with this expanded observational dataset (and with the same population-based priors
387 and background estimates) show slightly higher global emissions, especially from tropical Asia,
388 during the ATom period (Fig. 7). Besides inclusion of additional observations, we also considered
389 an alternative background estimate (background 2) that was calibrated to the global CFC-11
390 emission estimates with alternative atmospheric lifetimes (54 and 56 years) (Montzka et al., 2021)
391 (Table S1). As expected, the derived global and regional emissions were lower with a background
392 calibrated to a longer atmospheric lifetime. However, the derived regional contributions to the
393 global CFC-11 emissions and emission changes between the HIPPO and ATom periods were
394 consistent with results considering a shorter lifetime (Fig. 7).
395   Results discussed so far were based on prior emissions with zero changes between the
396 HIPPO and ATom periods for all regions considered. The remaining questions are whether the
397 derived near-zero emission changes over North America, South America, Africa, Europe, and
398 Australia were due to the influence from prior assumption (of zero emission changes) or if they
399 were constrained by the atmospheric observations. Another question is how much the derived
400 Asian emissions and emission changes are dependent on prior assumptions. To address these
401 questions, we constructed 14 additional emission priors that assumed 20 Gg yr^{-1} CFC-11 emission
402 increases between the HIPPO and ATom (7 priors) or 20 Gg yr^{-1} CFC-11 emission decreases
403 between both periods (another 7 priors; Table S1; Fig. 8). In the first 7 cases, we considered the

404 same population-based prior with a global CFC-11 emission of 67 Gg yr^{-1} during the HIPPO
405 period, whereas during the ATom period, we assumed there was an increase of 20 Gg yr^{-1} of CFC-
406 11 emissions over individual continents (*i.e.*, North America, South America, Africa, Europe,
407 Australia) or individual Asian subregions (*i.e.*, boreal Asia, temperate eastern Asia, temperate
408 western Asia, and tropical Asia) (Table S1; Fig. 8). In the latter 7 cases, we considered opposite
409 scenarios, where we assumed 67 Gg yr^{-1} of emissions during the ATom period and 87 Gg yr^{-1} of
410 emissions during the HIPPO period, so that emissions over individual continents or individual
411 Asian subregions had a 20 Gg yr^{-1} decrease between both periods (Fig. 8). Note that, given we've
412 already know there was a global increase of CFC-11 emissions from 2010 to 2018 (Montzka et al.,
413 2021; Montzka et al., 2018) and 60 ± 40 % of this global increase was from eastern mainland
414 China (Park et al., 2021; Rigby et al., 2019), many of the assumed 14 prior cases were quite
415 unrealistic. However, such extreme cases helped for estimating uncertainties that truly reflect the
416 capability of the selected atmospheric measurements for constraining continental and regional
417 emissions and their change through time. In all of the 14 extreme cases, regional emissions and
418 emission changes derived for the northern hemispheric lands, i.e., Asia, North America, Europe,
419 were consistent (Fig. 8). Derived regional emissions and emission changes for the southern
420 hemispheric lands, such as South America, Africa, Australia, however, show a strong dependence
421 on prior assumptions, especially during the ATom period (Fig. 8). The strong dependence of
422 inversion-derived emissions over the southern hemispheric lands were due to large sampling gaps
423 and small sensitivity to emissions from these regions (Fig. 1).
424   Summarizing emissions derived from all 23 inversion ensembles (Table 1; Figs. 6 - 8), our
425 results suggest the relatively remote observations provide important constraints on regional
426 emissions from North America, Asia, and Europe, as the derived ranges of posterior emissions
427 were smaller than the ranges of prior emissions considered for these regions (Figs. 6 - 8). The
428 only continent that shows a statistically significant increase of CFC-11 emissions is Asia, where
429 the best estimate of these 23 cases suggests an increase of 24 (18 – 28) Gg yr^{-1} of CFC-11 emissions
430 (the 2.5^{th} – 97.5^{th} percentile range) (Table 1), accounting for 86 (59 – 115) % of the global CFC-
431 11 emission increases between the HIPPO and ATom periods. All the best estimates from the 23
432 inversion ensembles suggest CFC-11 emission increases not only from temperate eastern Asia, but
433 also from temperate western Asia and tropical Asia. However, if we consider the entire range of
434 uncertainties (the range of best estimates and 2σ errors from each inversion), the derived emission
435 increases were statistically insignificant at the subregion level (i.e., temperate eastern Asia,
436 temperate western Asia, and tropical Asia).
437   Our results also suggest inverse modeling of the relatively remote observations we
438 considered here provided only weak constraints on emissions from the southern hemispheric
439 continents, i.e., South America, Africa, and Australia. Although we cannot eliminate the
440 possibility of some increase in CFC-11 emissions from these southern hemispheric regions based
441 on atmospheric inversion analyses alone, they did not account for the majority of the emission
442 increase. This is because during 2010 – 2018, when the global CFC-11 emissions increased, so
443 did the north-to-south mole fraction difference between the hemispheres (Montzka et al., 2021),
444 which indicates the emission increase occurred predominantly in the northern hemisphere.
445
446 **3.2.3. Comparison of regional emission estimates from other top-down analyses**
447   Our regional emission estimates of CFC-11 from the global atmospheric CFC-11
448 measurements made far away from the emissive regions are in a broad agreement with those

449 estimated from atmospheric observations made closely downwind of the emissive regions (Table
450 2), which had atmospheric CFC-11 enhancements that were one-two orders of magnitude larger
451 than those used in this inversion analysis (Park et al., 2021; Rigby et al., 2019; Hu et al., 2017;
452 Fraser et al., 2020). Emissions estimated for eastern mainland China using measurements made
453 in South Korea were $5 - 13$ Gg yr^{-1} during $2010 - 2011$ and $12 - 20$ Gg yr^{-1} during 2016 - 2017,
454 considering the full range of estimates from multiple inversion systems with different transport
455 simulations (Park et al., 2021). CFC-11 emission estimates for eastern China based on
456 measurements made in Taiwan were $14 - 23$ Gg yr^{-1} during $2014 - 2018$ (Adcock et al., 2020). In
457 the current analysis, we estimated CFC-11 emissions from temperate eastern Asia were $5 - 16$ Gg
458 yr^{-1} during Nov 2009 – Sep 2011 and $9 - 22$ Gg yr^{-1} during August 2016 – May 2018, which agree
459 well with the published analyses over eastern China, although our definition of temperate eastern
460 Asia is slightly different from the regions defined in Rigby et al. (2019), Adcock et al. (2020) and
461 Park et al. (2021).

462   Previously, we estimated the US emissions of CFC-11 between 2008 and 2014 with more
463 extensive atmospheric measurements made from towers and aircraft sites from all vertical levels
464 over North America (Hu et al., 2017). In this analysis, we only used a subset of observations (only
465 aircraft observations above 1 km above ground) and a coarser resolution of transport models in the
466 global inversion. While the North American CFC-11 emissions derived here are likely not as
467 accurate; they did agree within uncertainties with our previous US estimates (Table 2).

468   Furthermore, CFC-11 emissions derived for Australia are also comparable with estimates
469 reported by Fraser et al. (2020) using measurements made in Australia (Table 2). Both suggest
470 CFC-11 emissions from Australia were less than 1 Gg yr^{-1} between 2009 and 2018. Contributions
471 from Australia to global CFC-11 emissions and emission changes were very small.

472   Besides temperate eastern Asia, North America, and Australia, we also compared our
473 derived European CFC-11 emissions for Nov 2009 – Sep 2011 with the value reported by Keller
474 et al. (2011) for western Europe in 2009. Our best estimate for all of Europe was about twice as
475 large as reported by Keller et al. (2011) for the western Europe, which only accounted for 40% of
476 the area we considered for all of Europe. If aggregating emissions from only grid cells considered
477 in Keller et al. (2011), the aggregated total emissions would be similar to the value reported by
478 Keller et al. (2011), although both studies focused on two different time periods (Table 2).

479   Other than the regions mentioned above, previous emission estimates for the rest of the
480 world are quite limited. Only one study quantified CFC-11 emissions from the northern and central
481 area of India in June 2016, reporting emissions of $\sim 1 - 3$ Gg yr^{-1} (Say et al., 2019). It is hard to
482 make a fair comparison with our analysis, given its short analysis period and a much smaller area
483 than our defined temperate western Asian region (Fig. 4). However, there was observational
484 evidence indicating likely strong regional emissions and a regional emission increase over
485 temperate western Asia between $2012 - 2017$. This was shown as substantially enhanced CFC-11
486 mole fractions observed in temperate western Asia for flask measurements made during $2012 -$
487 2018 (Simpson et al., 2019) and the slow-down of atmospheric CFC-11 decline retrieved from
488 satellite remote sensing measurements (Chen et al, 2020). Furthermore, in situ measurements
489 made in tropical Asia in 2017 (Lin et al., 2019) also indicate likely strong regional emissions of
490 CFC-11 over this area.

491
492
493

494 **4. Conclusions**
495   We used global atmospheric CFC-11 measurements primarily made over the Pacific and
496 Atlantic Ocean basins and in the free troposphere over North America to quantify changes in
497 continental-scale emissions between November 2009 - September 2011 and August 2016 – May
498 2018. These two periods covered the times when the global CFC-11 emissions were at their
499 minimum and maximum, respectively, in recent years, at least before the sharp decline noted after
500 2018 (Montzka et al., 2021). Atmospheric CFC-11 measurements made in the HIPPO and ATom
501 campaigns confirm that the slow-down of atmospheric CFC-11 mole fraction decline between
502 2009 and 2018 was present throughout the troposphere. The ATom campaign data further display
503 larger atmospheric CFC-11 enhancements in flights, particularly over the Pacific Ocean basin as
504 compared to the Atlantic Ocean basin, suggesting larger emissions in regions immediately upwind
505 of the Pacific Ocean than the Atlantic Ocean.
506   Inverse modeling of these global atmospheric CFC-11 measurements suggests three Asian
507 regions were primarily responsible for the global CFC-11 emission changes from 2009-11 to 2016-
508 18 in all of the 23 inversion ensembles, including various extreme initial assumptions of regional
509 CFC-11 emission changes ($\pm$ 20 Gg yr^{-1}) between both periods. Our results suggest that, during
510 November 2009 – September 2011, Asia emitted 24 (14 – 40) Gg yr^{-1} of CFC-11, accounting for
511 43 (37 – 52) % of the global emission (Table 1), whereas the Asian CFC-11 emissions increase to
512 48 (38 – 65) Gg yr^{-1} or 57 (49 - 62) % of the global emission during August 2016 – May 2018
513 (Table 1). In both periods, substantial CFC-11 emissions were derived for temperate eastern Asia,
514 temperate western Asia, and tropical Asia. Besides eastern mainland China, our results suggest
515 there could be increases of CFC-11 emissions from temperate western Asia and tropical Asia from
516 2010 to 2018, considering the range of best estimates from the 23 inversion ensembles. In contrast
517 to Asia, other continents accounted for relatively smaller fractions of global CFC-11 emissions in
518 both periods. Although for continents in the Southern Hemisphere, our inversion analyses only
519 provide weak constraints on the CFC-11 emission changes between 2012 and 2018. However,
520 significant increases in CFC-11 emissions from these regions are unlikely, given the observed
521 concurrent increase of the north-to-south difference in CFC-11 surface mole fractions.
522
523 **Acknowledgement**
529
530 **Code/Data availability:** NOAA atmospheric observations are available at the NOAA/GML
531 website (https://gml.noaa.gov/hats/). Data collected from ATom were available via
532 https://espo.nasa.gov/atom/content/ATom.   Data collected from HIPPO were available via
533 https://www.nsf.gov/news/news_summ.jsp?cntn_id=127003.   Inversion-derived continental
534 fluxes were tabulated and described in this paper. All analysis tools and computing code used in
535 this analysis will be available upon reasonable request.
536
537 **Author contributions**

538 LH and SAM designed the analysis; LH conducted inversions and wrote the paper; SAM led the
539 NOAA global flask measurements, HIPPO and ATom GCMS measurements, and provided
540 substantial input on the analyses and edits of this paper; FM and EH collected HIPPO and ATom
541 flask-air samples; GD led the CATS measurements and prepared CATS data for this analysis;
542 MCS made the NOAA flask measurements; LH and KT computed HYSPLIT footprints; RWP
543 conducted the WACCM simulations and provided the model results; KM conducted NOAA
544 aircraft data QA/QC; CW led the NOAA aircraft sampling network; IV led the Persus GCMS flask
545 measurements; DN helped with data QA/QC for CFC-11 flask measurements; BH led the
546 calibration for NOAA measurements; SW led the HIPPO and ATom campaigns; all authors
547 contributed to the editing of this paper.
548
549 **Competing interests:** the authors declare no competing interests.
550

551 **References**
552 Adcock, K. E., Ashfold, M. J., Chou, C. C. K., Gooch, L. J., Mohd Hanif, N., Laube, J. C., Oram,
553 D. E., Ou-Yang, C.-F., Panagi, M., Sturges, W. T., and Reeves, C. E.: Investigation of East Asian
554 Emissions of CFC-11 Using Atmospheric Observations in Taiwan, Environmental Science &
555 Technology, 54, 3814-3822, 10.1021/acs.est.9b06433, 2020.

556 Bourgeois, I., Peischl, J., Thompson, C. R., Aikin, K. C., Campos, T., Clark, H., Commane, R.,
557 Daube, B., Diskin, G. W., Elkins, J. W., Gao, R. S., Gaudel, A., Hintsa, E. J., Johnson, B. J., Kivi,
558 R., McKain, K., Moore, F. L., Parrish, D. D., Querel, R., Ray, E., Sánchez, R., Sweeney, C.,
559 Tarasick, D. W., Thompson, A. M., Thouret, V., Witte, J. C., Wofsy, S. C., and Ryerson, T. B.:
560 Global-scale distribution of ozone in the remote troposphere from the ATom and HIPPO airborne
561 field missions, Atmos. Chem. Phys., 20, 10611-10635, 10.5194/acp-20-10611-2020, 2020.

562 Chen, X., Huang, X., and Strow, L. L.: Near-Global CFC-11 Trends as Observed by Atmospheric
563 Infrared Sounder From 2003 to 2018, Journal of Geophysical Research: Atmospheres, 125,
564 e2020JD033051, https://doi.org/10.1029/2020JD033051, 2020.

565 Davis, N. A., Davis, S. M., Portmann, R. W., Ray, E., Rosenlof, K. H., and Yu, P.: A
566 comprehensive assessment of tropical stratospheric upwelling in the specified dynamics
567 Community Earth System Model 1.2.2 – Whole Atmosphere Community Climate Model (CESM
568 (WACCM)), Geosci. Model Dev., 13, 717-734, 10.5194/gmd-13-717-2020, 2020.

569 Dhomse, S. S., Feng, W., Montzka, S. A., Hossaini, R., Keeble, J., Pyle, J. A., Daniel, J. S., and
570 Chipperfield, M. P.: Delay in recovery of the Antarctic ozone hole from unexpected CFC-11
571 emissions, Nature Communications, 10, 5781, 10.1038/s41467-019-13717-x, 2019.

572 Engel, A., Rigby, M., Burkholder, J. B., Fernandez, R. P., Froidevaux, L., Hall, B. D., Hossaini,
573 R., Saito, T., Vollmer, M. K., and Yao, B.: Update on Ozone-Depleting Substances (ODSs) and
574 Other Gases of Interest to the Montreal Protocol, Chapter 1 in Scientific Assessment of Ozone
575 Depletion: 2018, World Meteorological Organization, Geneva, Switzerland, 2018.

576 Fraser, P. J., Dunse, B. L., Krummel, P. B., Steele, L. P., Derek, N., Mitrevski, B., Allison, C. E.,
577 Loh, Z., Manning, A. J., Redington, A., and Rigby, M.: Australian chlorofluorocarbon (CFC)
578 emissions: 1960–2017, Environmental Chemistry, 17, 525-544, https://doi.org/10.1071/EN19322,
579 2020.

Atmospheric
Chemistry
and Physics

Discussions

580 Hu, L., Montzka, S. A., Lehman, S. J., Godwin, D. S., Miller, B. R., Andrews, A. E., Thoning, K.,
581 Miller, J. B., Sweeney, C., Siso, C., Elkins, J. W., Hall, B. D., Mondeel, D. J., Nance, D., Nehrkorn,
582 T., Mountain, M., Fischer, M. L., Biraud, S. C., Chen, H., and Tans, P. P.: Considerable
583 contribution of the Montreal Protocol to declining greenhouse gas emissions from the United
584 States, Geophysical Research Letters, 44, 2017GL074388, 10.1002/2017GL074388, 2017.

585 Hu, L., Montzka, S. A., Miller, B. R., Andrews, A. E., Miller, J. B., Lehman, S. J., Sweeney, C.,
586 Miller, S. M., Thoning, K., Siso, C., Atlas, E. L., Blake, D. R., de Gouw, J., Gilman, J. B., Dutton,
587 G., Elkins, J. W., Hall, B., Chen, H., Fischer, M. L., Mountain, M. E., Nehrkorn, T., Biraud, S. C.,
588 Moore, F. L., and Tans, P.: Continued emissions of carbon tetrachloride from the United States
589 nearly two decades after its phaseout for dispersive uses, Proceedings of the National Academy of
590 Sciences, 113, 2880-2885, 10.1073/pnas.1522284113, 2016.

591 Hu, L., Montzka, S. A., Miller, J. B., Andrews, A. E., Lehman, S. J., Miller, B. R., Thoning, K.,
592 Sweeney, C., Chen, H., Godwin, D. S., Masarie, K., Bruhwiler, L., Fischer, M. L., Biraud, S. C.,
593 Torn, M. S., Mountain, M., Nehrkorn, T., Eluszkiewicz, J., Miller, S., Draxler, R. R., Stein, A. F.,
594 Hall, B. D., Elkins, J. W., and Tans, P. P.: U.S. emissions of HFC-134a derived for 2008–2012
595 from an extensive flask-air sampling network, Journal of Geophysical Research: Atmospheres,
596 2014JD022617, 10.1002/2014JD022617, 2015.

597 Keeble, J., Abraham, N. L., Archibald, A. T., Chipperfield, M. P., Dhomse, S., Griffiths, P. T., and
598 Pyle, J. A.: Modelling the potential impacts of the recent, unexpected increase in CFC-11
599 emissions on total column ozone recovery, Atmos. Chem. Phys., 20, 7153-7166, 10.5194/acp-20-
600 7153-2020, 2020.

601 Keller, C. A., Brunner, D., Henne, S., Vollmer, M. K., O'Doherty, S., and Reimann, S.: Evidence
602 for under-reported western European emissions of the potent greenhouse gas HFC-23,
603 Geophysical Research Letters, 38, L15808, 10.1029/2011gl047976, 2011.

604 Lin, Y., Gong, D., Lv, S., Ding, Y., Wu, G., Wang, H., Li, Y., Wang, Y., Zhou, L., and Wang, B.:
605 Observations of High Levels of Ozone-Depleting CFC-11 at a Remote Mountain-Top Site in
606 Southern China, Environmental Science & Technology Letters, 6, 114-118,
607 10.1021/acs.estlett.9b00022, 2019.

608 Marsh, D. R., Mills, M. J., Kinnison, D. E., Lamarque, J.-F., Calvo, N., and Polvani, L. M.: Climate
609 Change from 1850 to 2005 Simulated in CESM1(WACCM), Journal of Climate, 26, 7372-7391,
610 10.1175/jcli-d-12-00558.1, 2013.

611 Michalak, A. M., Hirsch, A., Bruhwiler, L., Gurney, K. R., Peters, W., and Tans, P. P.: Maximum
612 likelihood estimation of covariance parameters for Bayesian atmospheric trace gas surface flux
613 inversions, Journal of Geophysical Research: Atmospheres, 110, D24107, 10.1029/2005jd005970,
614 2005.

615 Montzka, S. A., Dutton, G. S., Yu, P., Ray, E., Portmann, R. W., Daniel, J. S., Kuijpers, L., Hall,
616 B. D., Mondeel, D., Siso, C., Nance, J. D., Rigby, M., Manning, A. J., Hu, L., Moore, F., Miller,
617 B. R., and Elkins, J. W.: An unexpected and persistent increase in global emissions of ozone-
618 depleting CFC-11, Nature, 557, 413-417, 10.1038/s41586-018-0106-2, 2018.

619 Montzka, S. A., Dutton, G. S., Portmann, R. W., Chipperfield, M. P., Davis, S., Feng, W.,
620 Manning, A. J., Ray, E., Rigby, M., Hall, B. D., Siso, C., Nance, J. D., Krummel, P. B., Mühle, J.,
621 Young, D., O'Doherty, S., Salameh, P. K., Harth, C. M., Prinn, R. G., Weiss, R. F., Elkins, J. W.,

14

Walter-Terrinoni, H., and Theodoridi, C.: A decline in global CFC-11 emissions during 2018−2019, Nature, 590, 428-432, 10.1038/s41586-021-03260-5, 2021.

Nehrkorn, T., Eluszkiewicz, J., Wofsy, S., Lin, J., Gerbig, C., Longo, M., and Freitas, S.: Coupled weather research and forecasting–stochastic time-inverted lagrangian transport (WRF–STILT) model, Meteorology and Atmospheric Physics, 107, 51-64, 10.1007/s00703-010-0068-x, 2010.

Park, S., Western, L. M., Saito, T., Redington, A. L., Henne, S., Fang, X., Prinn, R. G., Manning, A. J., Montzka, S. A., Fraser, P. J., Ganesan, A. L., Harth, C. M., Kim, J., Krummel, P. B., Liang, Q., Mühle, J., O'Doherty, S., Park, H., Park, M.-K., Reimann, S., Salameh, P. K., Weiss, R. F., and Rigby, M.: A decline in emissions of CFC-11 and related chemicals from eastern China, Nature, 590, 433-437, 10.1038/s41586-021-03277-w, 2021.

Ray, E. A., Portmann, R. W., Yu, P., Daniel, J., Montzka, S. A., Dutton, G. S., Hall, B. D., Moore, F. L., and Rosenlof, K. H.: The influence of the stratospheric Quasi-Biennial Oscillation on trace gas levels at the Earth's surface, Nature Geoscience, 13, 22-27, 10.1038/s41561-019-0507-3, 2020.

Rigby, M., Park, S., Saito, T., Western, L. M., Redington, A. L., Fang, X., Henne, S., Manning, A. J., Prinn, R. G., Dutton, G. S., Fraser, P. J., Ganesan, A. L., Hall, B. D., Harth, C. M., Kim, J., Kim, K. R., Krummel, P. B., Lee, T., Li, S., Liang, Q., Lunt, M. F., Montzka, S. A., Mühle, J., O'Doherty, S., Park, M. K., Reimann, S., Salameh, P. K., Simmonds, P., Tunnicliffe, R. L., Weiss, R. F., Yokouchi, Y., and Young, D.: Increase in CFC-11 emissions from eastern China based on atmospheric observations, Nature, 569, 546-550, 10.1038/s41586-019-1193-4, 2019.

Rodgers, C. D.: Inverse Methods for Atmospheric Sounding, World Sci., Oxford, 10.1142/3171, 2000.

Say, D., Ganesan, A. L., Lunt, M. F., Rigby, M., O'Doherty, S., Harth, C., Manning, A. J., Krummel, P. B., and Bauguitte, S.: Emissions of halocarbons from India inferred through atmospheric measurements, Atmos. Chem. Phys., 19, 9865-9885, 10.5194/acp-19-9865-2019, 2019.

Simpson, I. J., Blake, D. R., Barletta, B., Meinardi, S., Blake, N. J., Wang, T., Yang, L., Stone, E. A., Yokelson, R. J., Farrukh, M. A., Aburizaiza, O. S., Khwaja, H., Siddique, A., Zeb, J., Woo, J. H., Kim, Y., Diskin, G. S., and Peterson, D. A.: Recent CFC-11 Enhancements in China, Nepal, Pakistan, Saudi Arabia and South Korea, American Geophysical Union, Fall Meeting 2019, San Francisco, CO, USA, December 01, 2019, 2019AGUFM.A33T2896S, A33T-2896, 2019.

Stein, A. F., Draxler, R. R., Rolph, G. D., Stunder, B. J. B., Cohen, M. D., and Ngan, F.: NOAA's HYSPLIT atmospheric transport and dispersion modeling system, Bulletin of the American Meteorological Society, 10.1175/BAMS-D-14-00110.1, 2015.

United Nations Environment Programme (UNEP): Executive Committee of the Multilateral Fund for the Implementation of the Montreal Protocol, Eighty-third Meeting. Addendum: Reports On Projects With Specific Reporting Requirements., 2019.

United Nations Environment Programme (UNEP): Consumption of controlled substances [dataset], 2021a.

United Nations Environment Programme (UNEP): Production of controlled substances [dataset], 2021b.

663   Wofsy, S. C., S. Afshar, H.M. Allen, E.C. Apel, E.C. Asher, B. Barletta, J. Bent, H. Bian, B.C.
664   Biggs, D.R. Blake, N. Blake, I. Bourgeois, C.A. Brock, W.H. Brune, J.W. Budney, T.P. Bui, A.
665   Butler, P. Campuzano-Jost, C.S. Chang, M. Chin, R. Commane, G. Correa, J.D. Crounse, P. D.
666   Cullis, B.C. Daube, D.A. Day, J.M. Dean-Day, J.E. Dibb, J.P. DiGangi, G.S. Diskin, M. Dollner,
667   J.W. Elkins, F. Erdesz, A.M. Fiore, C.M. Flynn, K.D. Froyd, D.W. Gesler, S.R. Hall, T.F. Hanisco,
668   R.A. Hannun, A.J. Hills, E.J. Hintsa, A. Hoffman, R.S. Hornbrook, L.G. Huey, S. Hughes, J.L.
669   Jimenez, B.J. Johnson, J.M. Katich, R.F. Keeling, M.J. Kim, A. Kupc, L.R. Lait, J.-F. Lamarque,
670   J. Liu, K. McKain, R.J. Mclaughlin, S. Meinardi, D.O. Miller, S.A. Montzka, F.L. Moore, E.J.
671   Morgan, D.M. Murphy, L.T. Murray, B.A. Nault, J.A. Neuman, P.A. Newman, J.M. Nicely, X.
672   Pan, W. Paplawsky, J. Peischl, M.J. Prather, D.J. Price, E.A. Ray, J.M. Reeves, M. Richardson,
673   A.W. Rollins, K.H. Rosenlof, T.B. Ryerson, E. Scheuer, G.P. Schill, J.C. Schroder, J.P. Schwarz,
674   J.M. St.Clair, S.D. Steenrod, B.B. Stephens, S.A. Strode, C. Sweeney, D. Tanner, A.P. Teng, A.B.
675   Thames, C.R. Thompson, K. Ullmann, P.R. Veres, N. Vieznor, N.L. Wagner, A. Watt, R. Weber,
676   B. Weinzierl, P.O. Wennberg, C.J. Williamson, J.C. Wilson, G.M. Wolfe, C.T. Woods, and L.H.
677   Zeng: ATom: Merged Atmospheric Chemistry, Trace Gases, and Aerosols [dataset],
678   https://doi.org/10.3334/ORNLDAAC/1581, 2018.

679
680
681
682
683
684
685
686
687
688
689
690
691
692
693
694
695
696
697
698
699
700
701
702
703
704
705
706
707

Table 1. Global and regional emissions (Gg yr^{-1}) derived from this analysis for Nov 2009 – Sep 2011 and Aug 2016 – May 2018 and the derived emission increases between the two periods (left columns). Two types of uncertainties were given in the parentheses. The former range indicates the 2.5th – 97.5th percentile range of the best estimates derived from the 23 inversion ensembles. The latter range indicates the 2.5th – 97.5th percentile range of the best estimates with their 2σ analytical uncertainties from each inversion ensemble member. The right columns indicate the fractional contributions of regional emission to the global CFC-11 emissions and emission changes. Values in the parentheses for the right columns indicate the 2.5th – 97.5th percentile range from the 23 inversion ensembles. Definitions of various regions are shown in Fig. 3.

Region	Nov 2009 - Sep 2011		Aug 2016 - May 2018		Change	
	Emissions	Percentage	Emissions	Percentage	Emissions	Percentage
Global	56 (49 – 68; 39 - 75)	100	84 (78 – 101; 67 – 113)	100	29 (21 – 40; 5 – 56)	100
Continents						
N. America	5.9 (5.6 – 7.1; 4.4 - 8.5)	11 (9 - 14)	5.6 (5.1 – 7.5; 3.5 – 9.6)	7 (6 - 9)	-0.4 (-2 – 1; -4 - 4)	-1 (-5 - 5)
S. America	6 (5 – 10; 1 - 16)	11 (9 - 16)	9 (7 – 18; 3 - 25)	11 (8 - 18)	3 (-2 – 11;-9 – 19)	8 (-9 - 27)
Africa	10 (7 – 14; 1 - 23)	17 (13 - 24)	9 (7 – 14; 2 - 24)	11 (8 - 15)	-1 (-6 – 5; -17 – 15)	-3 (-26 - 14)
Asia	24 (21 – 33; 14 - 40)	43 (37 - 52)	48 (45 – 56; 38 - 65)	57 (49 - 62)	24 (18 – 28; 8 - 39)	86 (59 - 115)
Europe	9 (5 – 11; 2 - 15)	15 (11 - 20)	11 (7 – 15; 4 - 18)	12 (9 - 16)	2 (-2 – 5; -7 - 10)	7 (-7 - 19)
Australia	0.5 (0.4 – 2; -1 - 4)	1 (1-3)	1 (0.6 – 6; 0.1 - 10)	1 (1-7)	0.7 (-1 – 6; -4 - 11)	2 (-4 - 16)
Asian Subregions						
Boreal Asia	0.6 (0.2 – 3; 0.1 - 5)	1 (0 - 6)	0.8 (0.4 – 3; 0.1 - 4)	1 (0 - 3)	0.1 (-3 – 2; -4 - 4)	0 (-11 - 8)
Temperate E. Asia	10 (8 – 13; 5 – 16)	18 (15 - 21)	14 (12 – 18; 9 - 22)	17 (14 - 23)	4 (2 – 8; -3 - 12)	15 (6 - 34)
Temperate W. Asia	6 (4 – 10; -3 - 16)	10 (7 - 14)	16 (12 – 20; 5 - 29)	19 (15 - 23)	10 (6 – 13; -3 - 24)	36 (25 - 56)
Tropical Asia	8 (6 – 11; 2 - 16)	14 (11 - 18)	18 (16 – 23; 11 - 29)	21 (17 - 25)	10 (5 – 14; -2 - 22)	35 (22 - 51)

717
718
719
720
721
722
723
724
725
726
727
728

17

729 **Table 2.** Comparison of regional emissions derived from this study and reported by previous top-
730 down analyses.

Regions	Time Periods	Emissions (Gg/y)	References
Asia			
Eastern Mainland China	2008 - 2012	5 – 13 [1]	Rigby et al., 2019; Park et al., 2021
Temperate Eastern Asia	Nov 2009 - Sep 2011	10 (5 - 16)	This Study
Eastern Mainland China	2014 - 2017	12 – 20 [1]	Rigby et al., 2019; Park et al., 2021
Eastern China	2014 - 2018	19 $\pm$ 5	Adcock et al., 2020
Temperate Eastern Asia	Aug 2016 - May 2018	14 (9 - 22)	This Study
Europe			
35° - 55°N; -10° - 30°E	2009	4.2 (2.9 - 5.4)	Keller et al., 2011
35° - 70°N; -10° - 60°E	Nov 2009 - Sep 2011	10 (6 - 16)	This Study
Australia			
Australia	2010 - 2017	0.32 $\pm$ 0.04	Fraser et al., 2021
Australia	Nov 2009 - Sep 2011	0.4 (0 - 0.8)	This study
Australia	Aug 2016 - May 2018	0.6 (0.1 - 1.6)	This study
North America			
The contiguous US	2009 - 2011	8.2 $\pm$ 1.0	Hu et al., 2017
North America	Nov 2009 - Sep 2011	5.9 (4.4 - 8.5)	This study
The contiguous US	2014	4.5 $\pm$ 0.7	Hu et al., 2017
North America	Aug 2016 - May 2018	5.6 (3.5 - 9.6)	This study

731 Notes: [1]values were taken from the reported inversion ensemble spread.
732
733
734
735
736
737
738
739
740
741
742
743
744
745
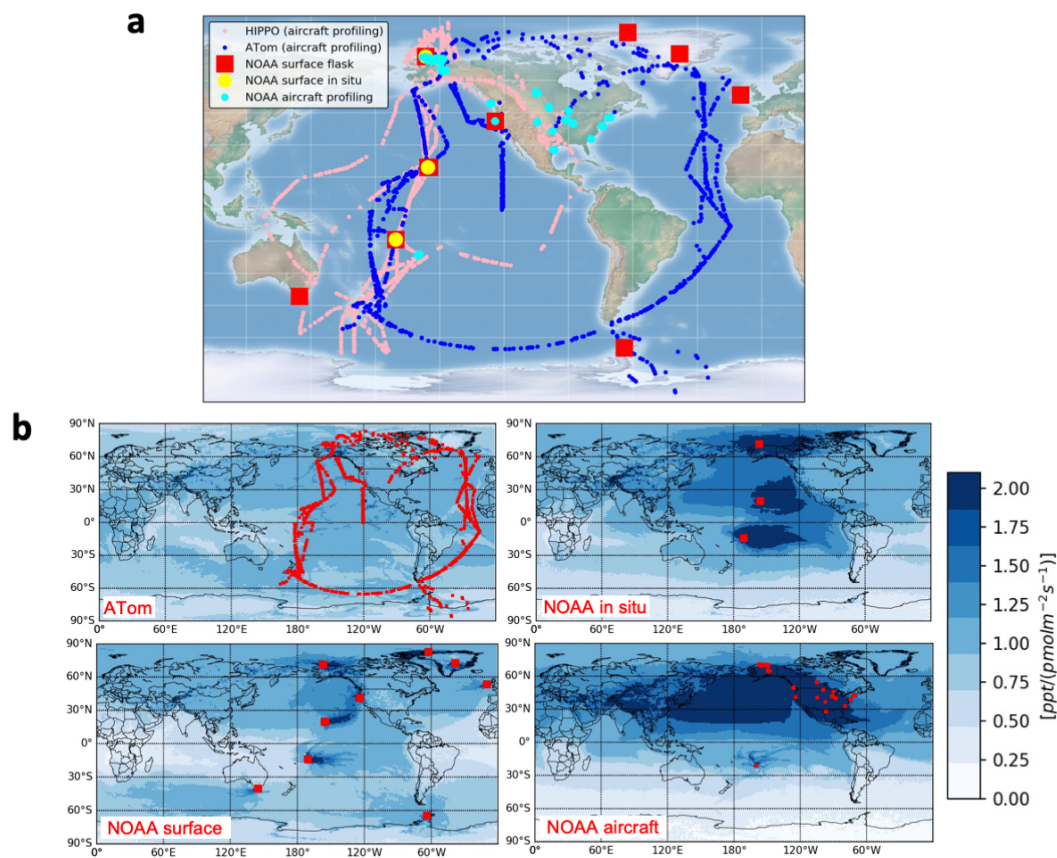
Fig. 1. Global atmospheric CFC-11 observations considered in this study, including flask measurements from the NASA HIPPO and ATom campaigns and the selected observations from the NOAA global weekly surface flask sampling network, NOAA global in situ surface sampling network, and NOAA aircraft profiling sites. The bottom panels indicate the summed footprints between Aug 2016 – May 2018 from ATom (number of observations: 1003), NOAA weekly surface flask network (number of observations: 781), in situ network (only selected 1 – 2 samples per day; number of observations: 2559), and biweekly – monthly aircraft profiling sites (only data above 1 km above ground were selected at North American sites; number of observations: 4824).
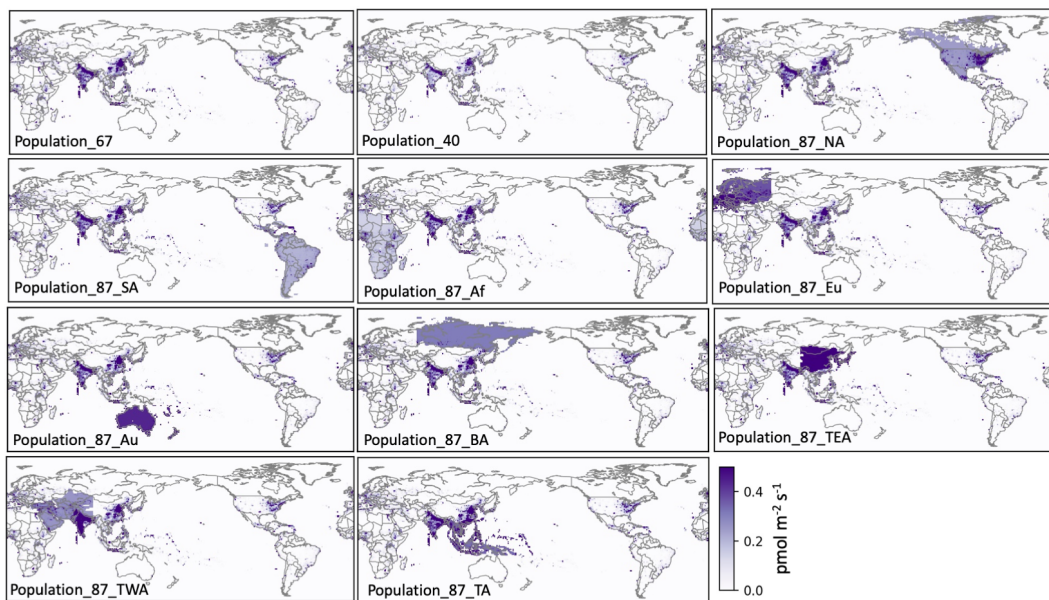
Fig. 2. Prior CFC-11 emissions used in this study. Priors of "population_67" and "population_40" have global CFC-11 emissions of 67 Gg yr^{-1} and 40 Gg yr^{-1}. Compared to the prior "population_67", priors of "population_87_NA", "population_87_SA", "population_87_Af", "population_87_Eu", "population_87_Au", "population_87_BA", "population_87_TEA", "population_87_TWA", and "population_87_TA" have a global emission total of 87 Gg yr^{-1} with additional 20 Gg yr^{-1} emissions imposed over North America, South America, Africa, Europe, Australia, boreal Asia, temperate eastern Asia, temperate western Asia, and tropical Asia, respectively.
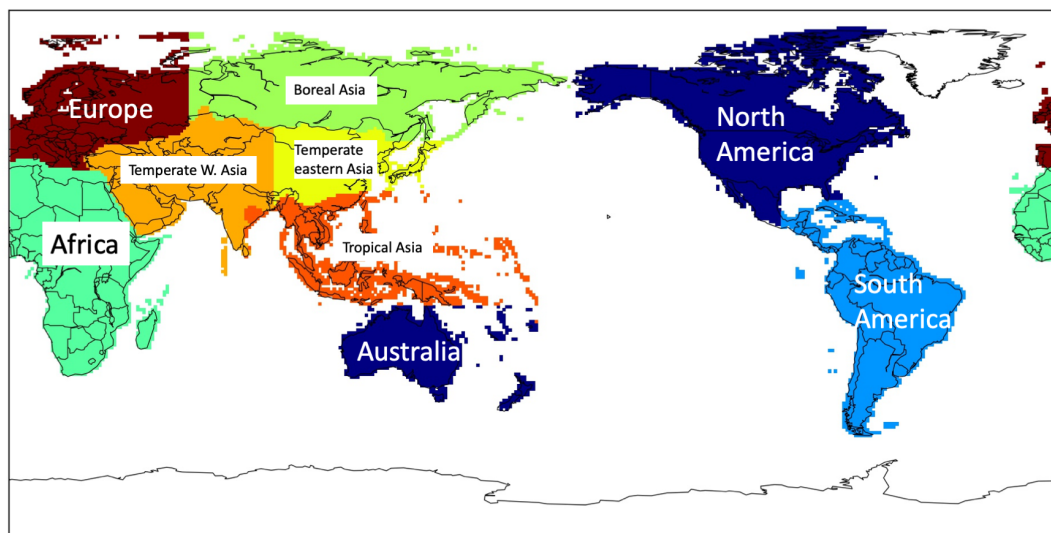
Fig. 3. Emissive regions defined for this analysis: North America, South America, Europe, Africa, Australia, and Asia; Asia was further divided into Boreal Asia, Temperate Eastern Asia, Temperate Western Asia, and Tropical Asia.
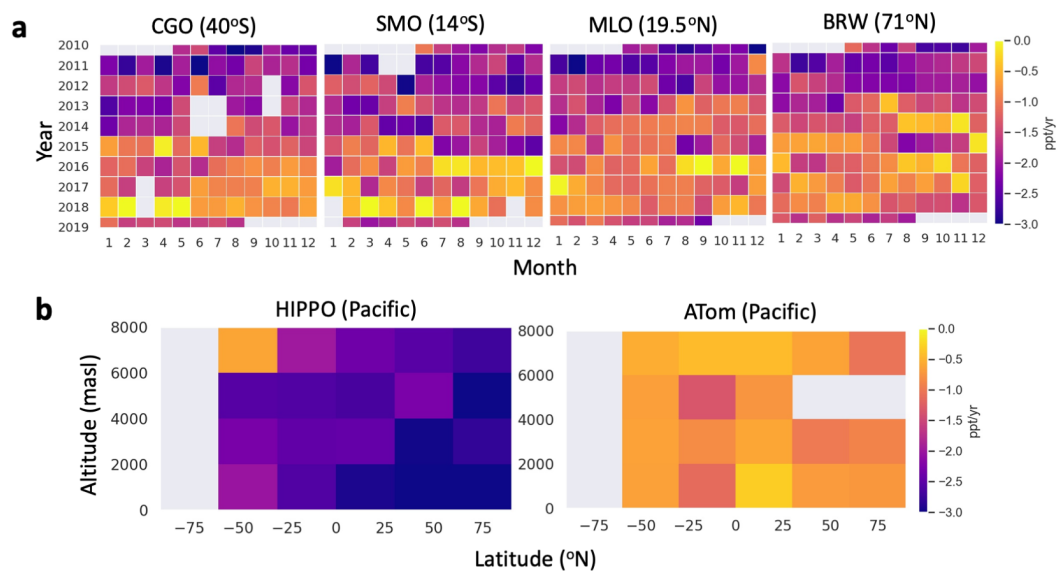
779
Fig. 4. Annual growth rates of atmospheric CFC-11 measured by four surface flask sampling sites
over the Pacific Ocean basin from 2010 – 2019 (a) and CFC-11 growth rates measured during the
HIPPO and ATom aircraft profiling surveys (b). Each cell indicates an annual difference relative
to the prior year for that given month (in panel a) or location (in panel b). Gray cells indicate
periods or locations with no data. The four surface sites plotted in panel (a) are at Cape Grim,
Tasmania, Australia (CGO), Tutuila, American Samoa (SMO), Mauna Loa, Hawaii, United States
(MLO), and Barrow, Alaska, United States (BRW).
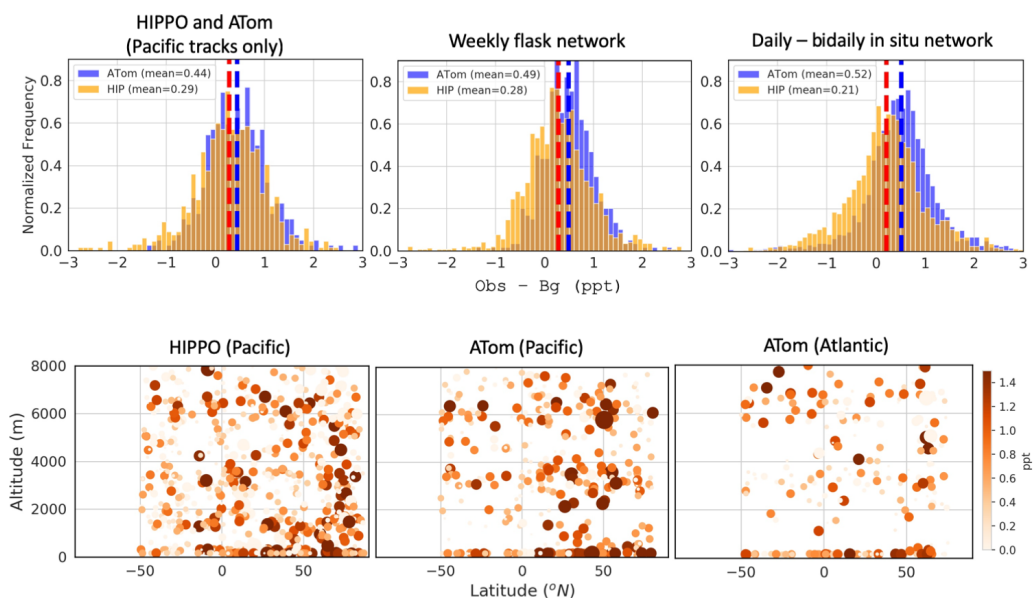
790
Fig. 5. Enhancements of CFC-11 mole fractions relative to background air mole fractions, measured by three independent networks during Nov 2009 – Sep 2011 (HIPPO period) and Aug 2016 – May 2018 (ATom period). (a) Histograms of enhancements of CFC-11 mole fractions measured from flasks collected over the Pacific Ocean basin during the HIPPO and ATom campaigns (left panel), in flasks collected in the NOAA weekly surface sampling network during those periods (middle panel), and measured from the NOAA in situ sampling network in both periods (right panel). Orange bars indicate normalized frequencies of enhancements observed in the HIPPO period, whereas blue bars indicate normalized frequencies of enhancements observed in the ATom period. Red and blue dashed lines denote the mean mole fractions observed during HIPPO and ATom periods. (b) Atmospheric CFC-11 mole fraction enhancements measured from flasks above the Pacific Ocean Basin during HIPPO (left) and ATom (middle), and above the Atlantic Ocean Basin during ATom (right). Both color shading and size of the symbols are proportional to the magnitude of mole fraction enhancements.
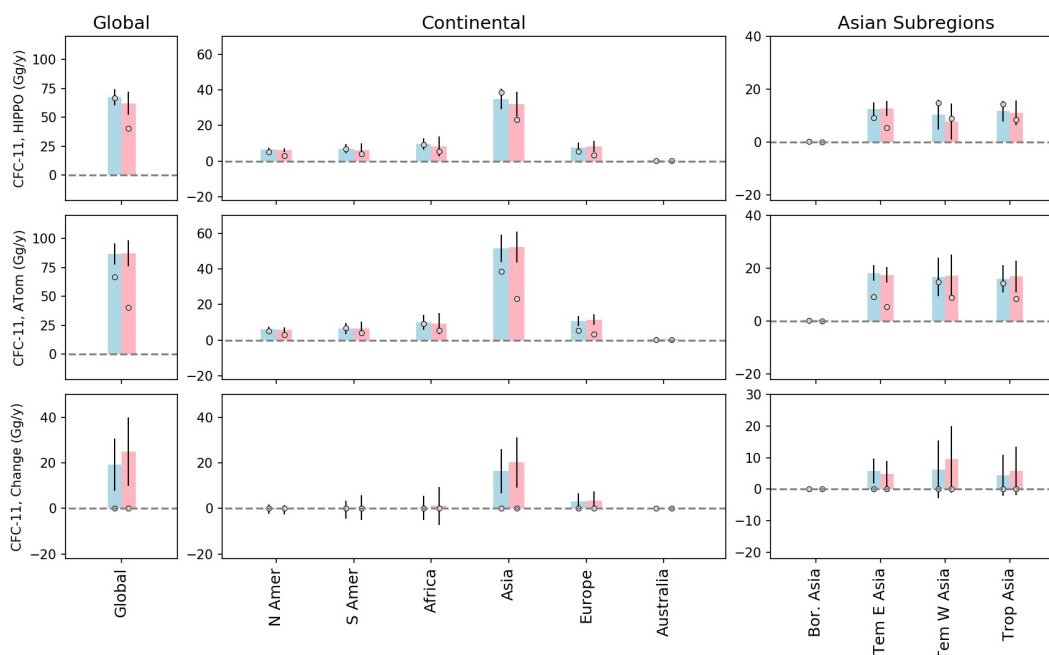
Fig. 6. Prior (circles) and posterior (bars) CFC-11 emissions derived for the globe, continents, and Asian subregions, from the "flask-only" inversions for the HIPPO period (upper three panels), the ATom period (middle three panels), and emission differences between the two periods (lower three panels). In each region and from the left to right, open circles denote the two assumed prior emissions ("population_67" and "population 40") with zero changes between the HIPPO and ATom periods; light blue and pink bars correspond to posterior emissions derived from the two different priors. Errorbars of CFC-11 emissions derived for the HIPPO and ATom periods (the upper and middle panels) indicate 2σ uncertainties derived from individual inversions. Errorbars for the derived CFC-11 emission changes (the lower panels) between the HIPPO and ATom periods were calculated from the sum of 2σ errors derived for the HIPPO and ATom inversions.

24
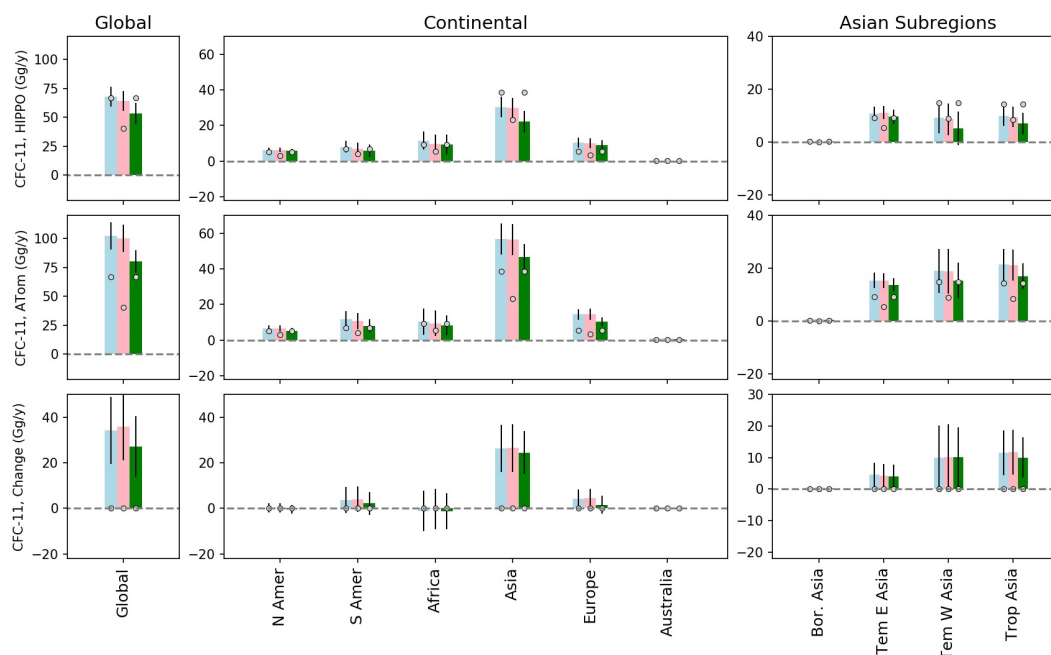
817
818 **Fig. 7.** Prior (circles) and posterior (bars) CFC-11 emissions derived for the globe, continents, and
819 Asian subregions, from the "flask + in situ" inversions for the HIPPO period (upper three panels),
820 the ATom period (middle three panels), and emission differences between the two periods (lower
821 three panels). In each region and from the left to right, open circles denote the three assumed prior
822 emissions ("population_67", "population 40", and "population_67") with zero changes between
823 the HIPPO and ATom periods; light blue, pink, and dark green bars indicate posterior emissions
824 derived from the three priors and two different background, as described in inversions ensembles
825 #3 - #5 in Table S1. Errorbars of CFC-11 emissions derived for the HIPPO and ATom periods
826 (the upper and middle panels) indicate 2σ uncertainties derived from individual inversions.
827 Errorbars for the derived CFC-11 emission changes between the HIPPO and ATom periods were
828 calculated from the sum of 2σ errors derived for the HIPPO and ATom inversions.
829
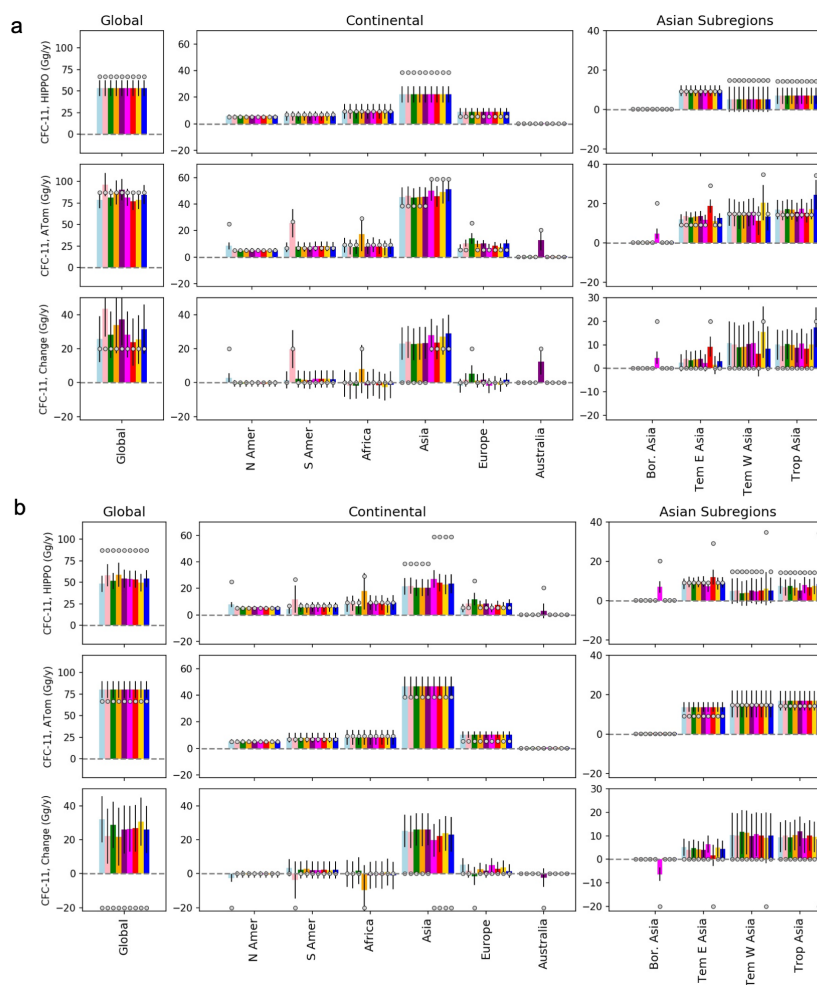
Fig. 8. Testing the sensitivity of assumed prior emission changes on the inversion-derived emission changes. (a) Assume a 20 Gg yr^{-1} emission increase between the HIPPO and ATom periods in individual continents and Asian subregions. (b) Assume a 20 Gg yr^{-1} emission decrease between the HIPPO and ATom periods in individual continents and Asian subregions. Similar to Fig. 7, posterior CFC-11 emissions were derived from the "flask + in situ" inversions for the HIPPO and the ATom periods. In each region and from the left to right, open circles denote the prior emissions as described for inversions ensembles #6 - #14 in Table S1 for panel (a), and for inversions ensembles #15 - #23 in Table S1 for panel (b); different color bars indicate the corresponding posterior emissions derived from inversions ensembles #6 - #14 (a) and ensembles #15 - #23 (b). Errorbars of CFC-11 emissions derived for the HIPPO and ATom periods indicate 2σ uncertainties derived from individual inversions. Errorbars for the derived CFC-11 emission changes between the HIPPO and ATom periods were calculated from the sum of 2σ errors derived for the HIPPO and ATom inversions.